IEEE Access
Multidisciplinary | Rapid Review | Open Access Journal

Received March 12, 2020, accepted March 24, 2020, date of publication March 30, 2020, date of current version April 15, 2020.

Digital Object Identifier 10.1109/ACCESS.2020.2984090

Intercalibration of FY-3C MWRI Against GMI Using the Ocean Microwave Radiative Transfer Model

ZI-QIAN ZENG, (Student Member, IEEE), AND GENG-MING JIANG, (Member, IEEE)
Key Laboratory for Information Science of Electromagnetic Waves (Ministry of Education), Fudan University, Shanghai 200433, China

Corresponding author: Geng-Ming Jiang (jianggm@fudan.edu.cn)

This work was supported by the National Key Research and Development Program of China under Grant 2018YFB0504900 and Grant 2018YFB0504902.

ABSTRACT This work addresses the intercalibration of the Microwave Radiation Imager (MWRI) on the Chinese second-generation polar-orbiting meteorological satellite Fengyun 3C (FY-3C) against the Microwave Imager (GMI) on the Global Precipitation Measurement (GPM) *Core Observatory*, in which a modified Double Difference (DD) method is developed and the Brightness Temperatures (TBs) in FY-3C MWRI and GMI channels are simulated using the ocean microwave Radiative Transfer Model (RTM) fed with the fifth generation of European Centre for Medium-range Weather Forecast (ECMWF) atmospheric reanalysis (ERA5) data. With the modified DD method, the intercalibration of FY-3C MWRI in 2017 are obtained. The results show that the MWRI observations are underestimated, especially for the low frequency channels. The calibration biases (mean of DDs) in FY-3C MWRI channels are temperature dependent, and decrease with the frequency increment. The in-orbit calibration of the MWRI descending (MWRID) data is 1∼2 K worse than that of the MWRI ascending (MWRIA) data. At the TBs of standard scene defined by the Global Space-based Inter-Calibration System (GSICS), the calibration errors (mean of DDs ± standard deviation at the mean) of MWRIA data in January 2017 are −6.7±0.4 K, −8.3±0.8 K, −3.0±0.7 K, −1.9±1.0 K, −2.5±1.1 K, −3.9±0.8 K, −2.1±1.5 K, −1.5±1.0 K and −0.4±2.3 K in the 10V/H, 18V/H, 23V, 36V/H and 89V/H channels, respectively, while the calibration errors of MWRID data in January 2017 are −7.6±0.8 K, −9.1±1.2 K, −4.4±0.8 K, −2.9±1.3 K, −3.6±1.2 K, −5.1±0.8 K, −2.6±1.4 K, −2.5±1.1 K and −1.2±2.5 K in the nine channels, respectively. Although calibration biases exist, the in-orbit calibration of FY-3C MWRI is generally stable in 2017. The results of the modified DD method are consistent with that of the DD method. The modified DD method is promising to be applied to the intercalibration with both target and reference radiometers on polar-orbiting satellites.

INDEX TERMS Intercalibration, FY-3C MWRI, GMI, ocean microwave radiative transfer model, the modified double difference method.

I. INTRODUCTION

Fengyun 3 (FY-3) series are the Chinese second-generation polar-orbiting meteorological satellites, and the third one, FY-3C, was launched into space from Taiyuan Satellite Launch Center on September 23, 2013. On FY-3C, there are thirteen remote sensing instruments: Earth Radiation Measurement - 1 (ERM-1), Global Navigation Satellite System Radio Occultation Sounder (GNOS), Infra-Red Atmospheric Sounder (IRAS), Medium Resolution Spectral Imager - 1 (MERSI-1), Micro-Wave Humidity Sounder - 2 (MWHS-2), Micro-Wave Radiation Imager (MWRI), Micro-Wave Temperature Sounder - 2 (MWTS-2), Solar Backscatter Ultraviolet Sounder (SBUS), Total Ozone Unit (TOU), Visible and Infra-Red Radiometer (VIRR), Solar Irradiance Monitor - 1 (SIM-1), Space Environment Monitor - High Energy Particle Detector (SEM/HEPD), and Space Environment Monitor - Ionosphere Measurement Sensor (SEM/IMS) (https://www.wmo-sat.info/oscar/satellites/view/ 115). Among these instruments, the MWRI is a total power passive microwave radiometer. It weighs 175 kilograms, and consists of an offset parabolic

The associate editor coordinating the review of this manuscript and approving it for publication was Mohamed Kheir.

main reflector with sizes of 97.74 cm × 89.7 cm. FY-3C MWRI has ten channels at frequencies of 10.65, 18.7, 23.8, 36.5 and 89 GHz with both vertical polarization (v-pol, V) and horizontal polarization (h-pol, V), hereafter named 10V/H, 18V/H, 23V/H, 36V/H, and 89V/H, respectively. A cold reflector and a hot reflector provide an end-to-end calibration system for the ten channels. FY-3C MWRI conically scans the Earth surfaces with an Earth Incidence Angle (EIA) of about 53.2°, and a swath of approximately 1400 km [1]–[3]. Table 1 lists the instrument parameters of FY-3C MWRI, including central frequency, bandwidth, polarization, Instantaneous Field of View (IFOV), and Noise-Equivalent Temperature Differences (NEΔT). According to the channel characteristics, the MWRI has the capability to monitor severe weather, such as typhoon, and convective clouds. The low frequency channels can penetrate clouds and provides forecasters with all-weather observations. For higher frequency channels, such as 89V/H, the scattering signatures from clouds and precipitation are also good indicators to detect rainfall over both land and ocean. The MWRI observations can be used to derive precipitation and cloud water, atmospheric precipitable water, Sea Surface Temperature (SST), soil moisture, soil temperature, snow cover and so on. Although FY-3C MWRI has an end-to-end calibration system, recent research reported that calibration biases exist in all the channels against the MWRI on the second FY-3 satellite (FY-3B), the Special Sensor Microwave Imager Sounder (SSMIS) and Tropical Rainfall Measuring Mission (TRMM) Microwave Imager (TMI) [3]. However, in [3], the differences of instrument parameters among these sensors, which have strong influence on the Brightness Temperature (TB) at top-of-atmosphere (TOA), were not taken into account, and thus the intercalibration results were inaccurate. Therefore, accurate assessment of the in-orbit calibration of FY-3C MWRI is necessary before further applications.

The other satellite radiometer that has similar instrument parameters to FY-3C MWRI is the Microwave Imager (GMI) on the Global Precipitation Measurement (GPM) *Core Observatory*, which was launched from the Tanegashima Space Center in Japan on 28 February 2014. With an orbit inclination of 65°, GPM extends observations into middle and high latitude. The GMI has thirteen microwave channels ranging between 10 GHz and 183 GHz. Both v-pol and h-pol observations are acquired at 10.65 (10V/H), 18.7 (18V/H), 36.64 (36V/H), 89.0 (89V/H) and 166.0 (166V/H) GHz, while only v-pol measurements are collected at 23.8 (23V), 183.31±7 (183±7V), and 183.31±3 (183±3V) GHz. The GMI conically scans the Earth surfaces with an EIA of about 52.8°. Besides the addition of high-frequency channels at 166, 183±3, and 183±7 GHz, the GMI also provides a number of improvements over other space-borne conically scanning radiometers, and the improvements include higher spatial resolution, and emphasis on calibration accuracy and stability. The instrument parameters of GMI are given in Table 2, and they are obviously different from that of FY-3C MWRI in Table 1, such as the central frequency and bandwidth. For calibration, the GMI is the first microwave imager to employ both external and internal calibration systems, and the dual calibration systems provide a way to measure the nonlinear response of the electronics in orbit. Recent research indicated that the GMI absolute calibration accuracy is about 0.25K 1-sigma bias over ocean, and exhibits remarkable long-term radiometric stability [4], [5]. The excellent performance of the GMI enables it to serve as both precipitation and radiometric standards for other GPM constellation members [6].

TABLE 1. Instrument parameters of the microwave radiation imager (MWRI) on Fengyun 3C (FY-3C).

No.	Channel name	Central frequency (GHz)	Bandwidth (MHz)	Polarization	NEΔT[a] (K)	IFOV[b] (km)
1/2	10V/H	10.65	180	V, H	0.5	51×85
3/4	18V/H	18.7	200	V, H	0.5	30×50
5/6	23V/H	23.8	400	V, H	0.8	27×45
7/8	36V/H	36.5	900	V, H	0.5	18×30
9/10	89V/H	89.0	2×2300	V, H	1.0	9×15

[a]NEΔT stands for noise equivalent temperature difference.
[b]IFOV denotes instantaneous field of view.

TABLE 2. Instrument parameters of the global precipitation measurement (GPM) microwave imager (GMI).

No.	Channel name	Central frequency (GHz)	Bandwidth (MHz)	Polarization	NEΔT (K)	IFOV (km)
1/2	10V/H	10.65	100	V, H	0.96	19×32
3/4	18V/H	18.7	200	V, H	0.84	11×18
5	23V	23.8	400	V	1.05	9.2×15
6/7	36V/H	36.64	1000	V, H	0.65	8.6×14
8/9	89V/H	89.0	6000	V, H	0.57	4.4×7.2
10/11	166V/H	166.0	4000	V, H	1.5	4.4×7.2
12	183±7V	183.31±7	2000	V	1.5	4.4×7.2
13	183±3V	183.31±3	2000	V	1.5	4.4×7.2

Accurate and stable calibration is a fundamental to quantitative remote sensing. To assess the calibration of an in-orbit instrument, there are mainly two methods: field calibration and intercalibration. The intercalibration is an operation that relates the observations of target sensor to the measurements of reference instrument [7], [8]. The basic premises of intercalibration are that the observations of target and reference sensors should be collocated in space and time with identical instrument parameters [9], [10], and additionally the in-orbit calibration of the reference instrument is accurate and stable. Because of its economic efficiency and easy implementation, intercalibration is popularly used, and many methods have been developed so far, such as the ray-matching method [3], [11]–[15], the Single Difference (SD) method [6], the Double Difference (DD) method [16], [17], the vicarious calibration method [18]–[20], etc. The ray-matching method directly compares the observations coincident in space and time to transfer the calibration from reference sensor to target instrument. However, the parameters of most of instruments aboard satellites are different, and as we know,

observations are function of instrument parameters. Therefore, the results obtained by the ray-matching method are usually inaccurate. Fortunately, the Radiative Transfer Model (RTM) has the capability to account for these differences on theoretical level by normalizing observations acquired by different instruments [11], [17]. Based on the RTM, the SD method first simulates TBs for non-precipitating scenes and then calculates the difference between observation and simulation for an individual radiometer. Although the SD method fully takes into account the instrument parameters, it is sensitive to simulation errors attributed to imperfect physics in the RTM and uncertainty in climate variables. The DD method employs coincident observations and simulations of two sensors under clear-sky conditions, and subtracts out both the simulation errors and expected sensor differences. Due to its excellent performance, the DD method has been used to intercalibrate the GPM microwave radiometer constellation by team within the GPM Intersatellite Calibration Working Group (XCAL) [6]. In order to collect large number of collocated observations between two radiometers, the DD method usually uses a large time window, typically 30∼60 minutes [6]. Our research revealed that the empirical filters [21]–[23] can only screen out part of cloud-contaminated observations, which may affect the results in high frequency channels. If the strict clear-sky criterion was used (see Section III for details), only about two hundreds of collocated observations over the $1^\circ \times 1^\circ$ gridded ocean surfaces between FY-3C MWRI and GMI were qualified in a month. In this case, the large time window may introduce errors into DDs, because both observations and simulations are functions of climate variables, which vary with time. Moreover, the number of qualified collocated observations will be dramatically reduced, if both the target and reference radiometers are aboard polar-orbiting satellites. The vicarious calibration method was originally developed in [18], and then refined by the National Aeronautics and Space Administration (NASA) Goddard Precipitation Processing System (PPS) for calibration of the GPM constellation [19], [20]. This technique relies on the stability of oversea histograms to calculate a cold reference TB, which is derived from observations of both target and reference radiometers, along with a cold reference TB from simulation. Different from the DD method, the vicarious calibration method does not require satellite observations coincident in space and time. However, the calibration is almost limited to the coldest end, because the reference TBs are obtained over sea surfaces with calm surface winds, no clouds, and minimal atmospheric water vapor.

In order to collect large number of qualified matching TBs with strict clear-sky criterion and reduce the errors due to residual clouds, a modified DD method is developed in this work, and then it is used to intercalibrate FY-3C MWRI against GMI. In the following, Section II presents the methodology; Section III describes the data and data processing; Section IV focuses on the results and analysis, and the last section is devoted to the conclusion and discussion.

II. METHODOLOGY

In [24]–[30], an ocean microwave RTM was developed (http://www.remss.com), and experimental results proved that this model has the capability to predict TB in a microwave channel to an accuracy of about 0.2 K and certainly better than 0.5 K [29]. The modified DD method in this work consists of an ocean microwave RTM and intercalibration equations. The ocean microwave RTM model is subdivided into Radiative Transfer Equation (RTE), atmospheric absorption model, and microwave Sea Surface Emissivity (SSE) model.

A. OCEAN MICROWAVE RADIATIVE TRANSFER EQUATION

Under clear-sky conditions, the TB at p polarization ($T_{B,p}$) observed by a microwave radiometer on orbiting satellite over ocean surface is given by the RTE [31]:

$$\begin{aligned} T_{B,p} &= T_{BU} + \tau \cdot E_p \cdot T_s + \tau \cdot T_{B\Omega} \\ T_{B\Omega} &= R_p \cdot [T_{BD} + \tau \cdot T_{cold}] + T_{B,scat,p} \end{aligned} \tag{1}$$

where T_s is SST, E_p is the SSE at p polarization. R_p is the sea surface reflectivity and equals to the complement of E_p, τ is the atmospheric transmittance, T_{BU} and T_{BD} are, respectively, the up- and down-welling atmospheric TBs. $T_{B\Omega}$ is the down-welling sky radiation that is scattered from sea surface, and T_{cold} is the effective cold space temperature after taking into account the deviation from the Rayleigh-Jeans approximation. $T_{B,scat,p}$ accounts for the atmospheric path length correction in the down-welling scattered sky radiation.

The atmospheric transmittance (τ) between heights s_1 and s_2 at an EIA, θ, is written as:

$$\tau(s_1, s_2) = \exp\left[-\sec(\theta)\int_{s_1}^{s_2} \alpha(h)dh\right] \tag{2}$$

The up- and down-welling atmospheric TBs are expressed by the integrals along the atmospheric path, respectively:

$$T_{BU} = \sec(\theta)\int_0^{TOA} \alpha(h)T(h)\tau(h, TOA)dh \tag{3a}$$

$$T_{BD} = \sec(\theta)\int_0^{TOA} \alpha(h)T(h)\tau(0, h)dh \tag{3b}$$

in which $\alpha(h)$ and $T(h)$ are the atmospheric absorption coefficient and atmospheric temperature at height h, respectively.

For a microwave channel, the quantities in the above equations are convolved over bandwidth to obtain the channel-averaged values.

B. ATMOSPHERIC ABSORPTION MODEL

In Eq. (1), the atmospheric transmittance, up- and down-welling atmospheric TBs are three key parameters to calculate the simulated TB.

According to electromagnetic wave theory, both phase and amplitude response of a plane radio wave propagating the distance z at frequency f are described by a field strength

$$E(z) = E(0)\exp\left[ikz\left(1 + N \times 10^{-6}\right)\right] \tag{4}$$

where $E(0)$ is the initial value, k is the free space wave number and equals to $2\pi f/c$, and c is the speed of light in vacuum. N is a complex refractivity of the atmospheric medium, and expressed by

$$N = N_0 + N' + iN'' \quad \text{ppm} \tag{5}$$

In Eq. (5), the real part of the complex refractivity changes the propagation velocity (refraction) and consists of a frequency-independent term, N_0, plus the dispersive refraction $N'(f)$. The imaginary part of the complex refractivity, N'', quantifies the atmospheric absorption coefficient, i.e.,

$$\alpha(h) = 0.04191 \times f \times N'' \quad \text{Nepers/km} \tag{6}$$

In the microwave spectrum below 100 GHz, atmospheric absorption comes from three components: oxygen, water vapor, and suspended water droplets or ice crystal [32]. The sum of these three components gives the total absorption coefficients. Numerous investigators have studied the dependence of the oxygen and water vapor coefficients on frequency, temperature, pressure and water vapor density [33]–[36], and extended the microwave spectrum up to 1000 GHz [35].

With the aid of laboratory measurements, Liebe *et al.* (1993) proposed a Millimeter-wave Propagation Model (MPM93) to describe the propagation characteristics of atmosphere for frequency from 1 to 1000 GHz. The refractivity of the main natural absorbers (oxygen, water vapor, suspended droplets and ice particles) are computed from known meteorological variables [33]–[36], and then the atmospheric transmittance, up- and down-welling atmospheric TBs in a microwave channel are calculated using Eq. (2) and Eq. (3). The MPM93 model is adopted in this work.

C. MICROWAVE SEA SURFACE EMISSIVITY

Another key parameter in the ocean microwave RTE is the microwave SSE (E_p). The SSE is mainly influenced by three types of sea roughness scales: large gravity waves, small gravity-capillary waves, and sea foam. Incorporating the first two roughness scales, numerous theoretical attempts have been made to model the SSE of wind-roughened sea surface with two-scale ocean surface models [37]–[41]. Unfortunately, none of them provides the needed level of accuracy [29]. In [29], a microwave SSE model between 6 and 90 GHz and over a large range of wind speeds (up to 40 m/s) and EIAs (up to 65°) for wind-roughed sea surface was developed using WindSat and Special Sensor Microwave Imager (SSM/I) observations. The microwave SSE consists of three components: the emissivity of the specular ocean surface (E_0), the isotropic wind-induced emissivity (ΔE_{W}), and four Stokes parameters of the wind direction signal (ΔE_φ), i.e.,

$$E_p = E_0 + \Delta E_W + \Delta E_\varphi \tag{7}$$

E_0 is the largest part. It depends on frequency (f), EIA (θ), T_{s} and salinity (S), and is related to the complex dielectric constant of seawater by means of the Fresnel equation.

The isotropic wind-induced emissivity depends on wind speed W, and its analytic form reads [29]

$$\begin{aligned}\Delta E_W = {} & \Delta E_W^{\mathrm{nad},f}(W, T_s, S) + [\Delta E_W^{p,f}(\theta_{\mathrm{ref}}, W, T_s, S) \\ & - \Delta E_W^{\mathrm{nad},f}(W, T_s, S)] \cdot \left(\frac{\theta}{\theta_{\mathrm{ref}}}\right)^{x_p}\end{aligned} \tag{8}$$

where $\Delta E_W^{\mathrm{nad},f}$ is the emissivity at nadir at frequency f, and θ_{ref} is the reference EIA and equals to 55.2°. For the exponents x_p (p = V/H), $x_{\mathrm{V}} = 4.0$ and $x_{\mathrm{H}} = 1.5$ at all frequencies and wind speed.

The four Stokes parameters of the wind direction signal ΔE_φ is expressed by the Fourier expansion with second order [29]

$$\Delta E_\varphi = \begin{cases} A_1^{p,f}(\theta; W) \cdot \cos(\varphi) + \\ A_2^{p,f}(\theta; W) \cdot \cos(2\varphi), & p = \mathrm{V}, \mathrm{H} \\ A_1^{p,f}(\theta; W) \cdot \sin(\varphi) + \\ A_2^{p,f}(\theta; W) \cdot \sin(2\varphi), & p = S3, S4 \end{cases} \tag{9}$$

in which φ is the wind direction relative to the azimuthal look (hereafter called Relative Azimuth Angle, RAA), and A_1 and A_2 are two coefficients.

More details about Eq. (7), Eq. (8) and Eq. (9) are given in [29]. Experimental results indicated that this model fits the independent measurements quite well, and can provide the needed level of accuracy for intercalibration [29].

D. IMPACT OF INSTRUMENT PARAMETERS ON BRIGHTNESS TEMPERATURE

As introduced in Section I, besides the differences of central frequency and bandwidth, the EIAs of FY-3C MWRI and GMI are also different, and they are about 53.2° and 52.8°, respectively. Moreover, the RAAs of FY-3C MWRI and GMI observations are usually not equal to each other. To investigate the impact of different instrument parameters on TBs at TOA, numerical experiments are carried out using the ocean microwave RTM fed with the SeeBor V5 training database (http://cimss.ssec.wisc.edu) [42]. The SeeBor V5 database, established by University of Wisconsin, consists of 15704 global profiles of temperature, moisture and ozone at 101 pressure levels for clear-sky conditions (relative humidity is less than 99% at all pressure levels), in which a total of 7275 profiles were collected over sea surfaces. Besides profiles at 101 pressure levels, the database also provides SST and wind speed. The experiments are conducted as follows. First, the microwave SSEs in the MWRI and GMI channels are modeled, in which the salinity is set to a fixed value of 35 ppt and RAA varies from 0° to 180° with a step of 30°. Then, the atmospheric transmittance, up- and down-welling TBs are calculated using MPM93, Eq. (2) and Eq. (3). Finally, the simulated TBs in FY-3C MWRI and GMI channels are computed using Eq. (1). As expected, the simulations in the MWRI and GMI channels with identical climate variables are not identical. To demonstrate the TB differences, Fig. 1 displays the histograms of the TB differences between FY-3C

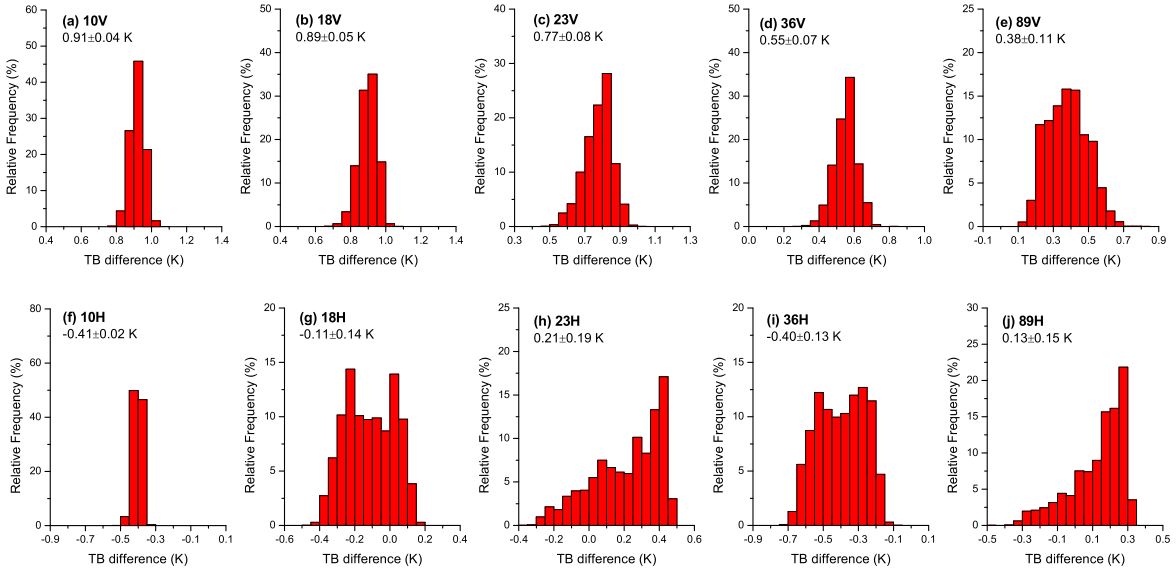

FIGURE 1. Histograms of brightness temperature differences between FY-3C MWRI and GMI simulations with identical RAAs and climate variables, but with different instrument parameters (the bin size = 0.05 K).

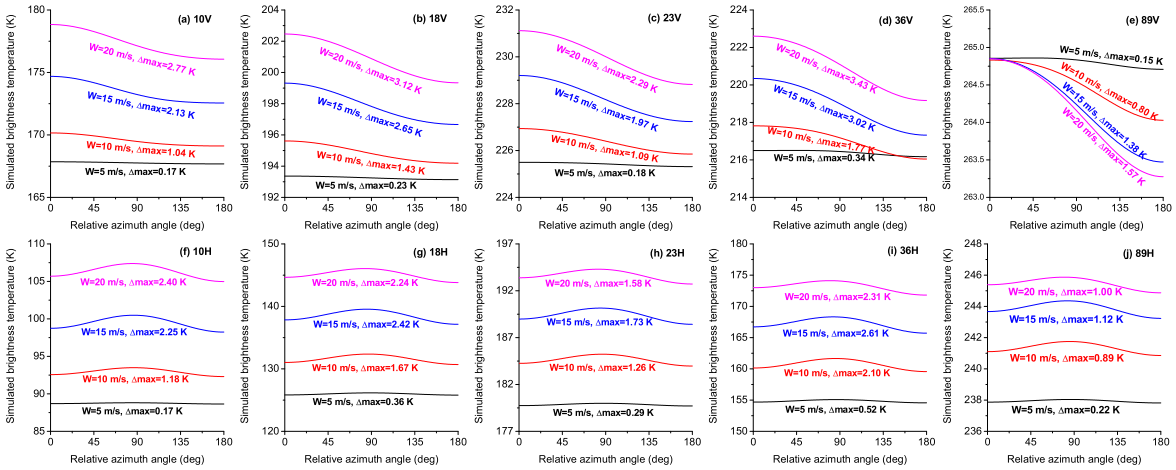

FIGURE 2. The simulated brightness temperatures in FY-3C MWI channels varying with wind speed (W) and relative azimuth angle (brightness temperatures are simulated using the ocean microwave RTM fed with the mid-latitude summer model atmosphere, and the Δ max denotes the maximum brightness temperature difference when relative azimuth angle goes from 0° to 180°).

MWRI and GMI simulations. The histograms are not centered at zero, and they are even asymmetric. Statistical results show that the TB differences (mean ± standard deviation at the mean) between FY-3C MWRI and GMI simulations are 0.91±0.04 K in the 10V channel, 0.89±0.05 K in the 18V channel, 0.77±0.08 K in the 23V channel, 0.55±0.07 K in the 36V channel, and 0.38±0.11 K in the 89V channel. Whereas they are −0.41±0.02 K, −0.11±0.14 K, 0.21±0.19 K, −0.40±0.13 K and 0.13±0.15 K in the five h-pol channels, respectively. The TB differences in the v-pol channels are larger than that in the h-pol channels, and they are too large to be ignored for intercalibration. These TB differences are totally attributed to the differences of instrument parameters between FY-3C MWRI and GMI.

To separate the influence of EIA difference, in the next numerical experiment, both the EIAs of FY-3C MWRI and GMI are set to 53.2°, and meanwhile the other parameters are unchanged. In this case, the TB differences between the MWRI and GMI simulations are purely due to the differences of central frequency and bandwidth. Statistical results indicate that the TB differences are 0.00±0.00 K in the 10V, 10H, 18V, 18H, 23V and 23H channels, whereas they are −0.24±0.01 K in the 36V channel, −0.40±0.01 K in the 36H channel, 0.00±0.01 K in the 89V channel, and −0.02±0.02 K in the 89H channel. The impact of bandwidth differences in the low frequency channels (≤23 GHz) is negligible. However, the TB differences in the 36V/H channels cannot be neglected, because both the

central frequency and bandwidth are obviously different (see Table 1 and Table 2).

Combining the above results, a conclusion can be made that the EIA difference between FY-3C MWRI and GMI has a significant impact on TBs, and meanwhile the influence of the central frequency and bandwidth differences in the high frequency channels cannot be ignored.

Note that, identical RAAs are used for both MWRI and GMI in the above simulations, but they are usually different in practice. To evaluate the impact of RAA on TBs, taking FY-3C MWRI as an example, another numerical experiment is conducted with the Mid-latitude Summer (MLS) model atmosphere. Actually, the impact of RAA on TBs is mainly attributed to sea surface wind speed (sea surface roughness). Four wind speeds, 5, 10, 15 and 20 m/s, are used in the simulation. Fig. 2 displays the FY-3C MWRI simulations varying with sea surface wind speed and RAA. Generally, the TBs in the MWRI v-pol channels gradually decrease when RAA varies from 0° to 180°, whereas the TBs in the MWRI h-pol channels present good symmetry: they firstly increase and reach its maximum at RAA of 90°, and then decrease. To quantify the relative impact, a maximum TB difference (Δ max) in a channel is calculated at given wind speed when RAA goes from 0° to 180° (Fig. 2). The Δ max is channel-dependent, and generally increases with wind speed. They are 0.17∼0.52 K at wind speed of 5 m/s, 1.04∼2.10 K at wind speed of 10 m/s, 1.73∼2.65 K at wind speed of 15 m/s, and 1.00∼3.43 K at wind speed of 20 m/s. Therefore, the influence of RAA on TBs cannot be neglected, especially for large sea surface wind speed.

E. INTERCALIBRATION EQUATIONS

First, the TBs in GMI channels under clear-sky conditions are simulated using the RTM fed with the climate variables of sea surface and atmosphere (SST, salinity, wind speed, wind direction, atmospheric temperature and humidity profiles), which are coincident with the GMI observations in space and time. Because of imperfect physics in the RTM and uncertainty in the associated climate variables, the simulations are usually not equal but approximate to the GMI observations. The bias between observation and simulation (O-B) is region-dependent, and it is also related to climate variables, such as water vapor, wind speed, and SST [23], [43]. In this work, the GMI is the reference radiometer, and thus the O-B biases between GMI observations and simulations should be removed. Statistical analysis in Section IV indicates that the observation in GMI channel i ($T_{\mathrm{GMI},i}$) is a linear/quadratic function of GMI simulations ($T_{\mathrm{GMI},j,\mathrm{RTM}}$, j=1,2,...9), SST, total column water vapor (WV), latitude (Lat) and wind speed (W).

$$T_{\mathrm{GMI},i} = \sum_{k=1}^{2}\left[\sum_{j=1}^{9}\left[a_{ijk}\left(T_{\mathrm{GMI},j,\mathrm{RTM}}\right)^k\right] + b_{ik}\left(T_s\right)^k + c_{ik}\left(WV\right)^k + d_{ik}\left(Lat\right)^k\right] + e_i \cdot W + f_i \quad (10)$$

where a_{ijk}, b_{ik}, c_{ik}, d_{ik}, e_i and f_i are unknown coefficients, which will be determined by multiple-variable regression on large number of TBs and climate variables coincident in space and time.

It should be noted that, because of fluctuation of satellite altitude and oblateness of the Earth, the EIA of GMI observations varies from 52.64° to 52.94°, and basically obeys a Gaussian distribution centered at 52.79°. We tried to add an EIA term in Eq. (10), but no improvement was obtained. To reduce the angular impact, the EIA is limited in a range between 52.74° and 52.84°, and about 70% of GMI observations fall into this range. If this range is replaced by the median EIA (52.79°), the maximum error is 0.12 K in all GMI channels, as indicated by numerical radiative transfer modeling experiment with the MLS model atmosphere. Therefore, the EIA is omitted in Eq. (10).

Once the coefficients in Eq. (10) are determined, from statistical point of view, the O-B biases in GMI channels are removed, and thus the theoretical observations in GMI channels can be predicted from the simulations and climate variables.

Then, the simulations in both FY-3C MWRI and GMI channels under clear-sky conditions are also calculated using the RTM fed with the climate variables collocated with FY-3C MWRI observations in space and time. It should be noted that, the RAAs of FY-3C MWRI observations are used for both MWRI and GMI simulations, and the EIA of GMI is set to a fixed value of 52.79°, which is the median EIA of GMI observations. The difference between FY-3C MWRI and GMI simulations, called the Simulated TB Difference (STD), is calculated. The STD does not contain the O-B biases, and only accounts for the differences of central frequency, bandwidth and EIAs between FY-3C MWRI and GMI.

Next, the theoretical observations in GMI channels are computed from the GMI simulations and climate variables coincident with FY-3C MWRI observations using Eq. (10). The difference between the actual observation of FY-3C MWRI and the theoretical observation of GMI, which defined as the Observed TB Difference (OTD) in this work, is calculated. The OTD contains both the TB differences attributed to the difference of instrument parameters and calibration bias between two radiometers. Finally, the DD is obtained by subtracting STD from OTD [43]

$$DD = OTD - STD \quad (11)$$

The mean values of DDs are the calibration biases of FY-3C MWRI, and they are usually functions of observations. To explicitly transfer calibration coefficients from GMI to FY-3C MWRI, an theoretical observation in the MWRI channel i ($T_{\mathrm{MWRI\_theoretical},i}$) is introduced in this work, and it equals to the difference between the actual observations

($T_{\mathrm{MWRI},i}$) and DD (DD_i) in the same channel,

$$T_{\mathrm{MWRI\_theoretical},i} = T_{\mathrm{MWRI},i} - DD_i \tag{12}$$

Combining Eq. (11) and Eq. (12), one can obtain

$$T_{\mathrm{MWRI\_theoretical},i} = T_{\mathrm{GMI\_theoretical},i} + STD \tag{13}$$

where $T_{\mathrm{GMI\_theoretical},i}$ is the theoretical observation of GMI.

Statistically, calibration biases are excluded from the theoretical observations in FY-3C MWRI channels. Assuming that the theoretical observations in the MWRI channels are quadratic functions of the actual observations, one can obtain

$$T_{\mathrm{MWRI\_theoretical},i} = A_i + B_{1,i} \times T_{\mathrm{MWRI},i} + B_{2,i} \times \left(T_{\mathrm{MWRI},i}\right)^2 \tag{14}$$

where A_i, $B_{1,i}$ and $B_{2,i}$ are intercalibration coefficients, which will be determined using regression.

III. DATA DESCRIPTION AND PROCESSING

The FY-3C MWRI L1 data (http://data.nsmc.org.cn), the GMI level 1C version 5 data (https://disc.gsfc.nasa.gov), and the fifth generation of European Centre for Medium-range Weather Forecast (ECMWF) atmospheric reanalysis (ERA5) data (https://cds.climate.copernicus.eu) over the entire Earth in 2017 are used in this work. Both FY-3C MWRI and GMI data provide TBs at TOA in all the channels, as well as the longitude, latitude, and viewing angles. In [44], a bias of about 2.0 K was found in FY-3C MWRI measurements between ascending and descending orbits using the O-B analysis. In [45], the physical parameters affecting the in-orbit calibration of FY-3C MWRI were analyzed, and it is found that the main reason leading to the bias between ascending and descending data is attributed to the high values of the hot reflector, which was heated periodically by incident solar radiation and thus emitted a variable radiation with space and time. Due to the ascending/descending difference, the operational FY-3C MWRI L1 data are grouped into two categories: ascending-orbit data and descending-orbit data with different calibration parameters, and hereafter they are called the MWRIA data and MWRID data, respectively. Note that, the GMI level 1C data do not contain incident azimuth angles, and they are calculated in terms of the positions of satellite and observations.

The ERA5 data provide hourly estimates of a large number of atmospheric, land and oceanic climate variables with longitude and latitude resolutions of $0.25° \times 0.25°$, and resolve the atmosphere using 37 levels from the surface up to a height of 80 km (https://cds.climate.copernicus.eu). The ERA5 climate variables used in this work include SST, wind speed and direction at 10 meters above sea surface, total cloud cover, geopotential profiles, atmospheric temperature and relative humidity profiles. The total cloud cover, ranging between 0 and 1, is a variable to give the ratio of the grid covered by clouds. When the total cloud cover is zero (clear-sky), the relative humidity is certainly less than 100% at all levels. However, it is not true on the contrary. This can be explained in this way: if the grid is partly cloud-contaminated (the total cloud cover is larger than zero), the relative humidity may be less than 100% because it is a mean value over the grid.

Previous research used empirical filters to screen out cloud-contaminated observations [21]–[23]. We tested these empirical filters, and found that only about 18% of matching observations between FY-3C MWRI and GMI were identified as cloudy ones. This violates the truth that about 60% of the Earth surfaces are covered by clouds. In a regular grid space with coarse longitude and latitude resolutions, e.g., $1° \times 1°$, the clear-sky observations are far less than 40%. This means that the empirical filters can only identify part of the cloud-contaminated observations, and the results in high frequency channels may be affected by residual clouds. In order to screen out the cloud-contaminated observations as far as possible, both the ERA5 total cloud cover and the empirical filters are used in this work.

The ERA5 data coincident with satellite observations in space and time are resampled into satellite swath space using the bilinear interpolation method. Under clear-sky conditions, the TBs at TOA in FY-3C MWRI and GMI channels are simulated using the RTM fed with the ERA5 data. To collect large number of qualified matching TBs between satellite observations and simulations, the following criteria are applied in a 3×3 neighborhood centered at a candidate matching point: ocean surfaces at least 75 km far away from land, the ERA5 total cloud cover of zero (clear-sky), absolute time difference between satellite observation and ERA5 data of less than 20 minutes, wind speed of less than 10 m/s, and SST of larger than 275.0 K.

Different from simulations, both FY-3C MWRI and GMI observations contain random noises. For homogenous sea surfaces and atmosphere, the simulations change little, whereas the satellite observations fluctuate due to random noises. This decreases the correlation between satellite observation and simulation. To reduce the influence of random noises, a low-pass filtering is applied: if the variation of simulations in the 10V channel in a connected region is less than 0.1 K, the mean values of both satellite observations and simulations in the region are calculated, and then they substitute for the original ones. As a result, the number of matching TBs is certainly reduced, however the correlation between satellite observation and simulation is increased.

The intercalibration procedure is divided into five steps. First, the GMI simulations under clear-sky conditions are calculated using the RTM fed with the ERA5 data coincident with GMI observations in space and time. Then, the coefficients in Eq. (10) are determined using multiple-variable regression. Next, the MWRI and GMI simulations under clear-sky conditions are computed using the RTM fed with the ERA5 data collocated with the MWRI observations in space and time, and STDs are calculated. Afterward, the theoretical observations in GMI channels coincident with the MWRI observations are predicted using Eq. (10), and the OTDs are calculated. Finally, the DDs and theoretical

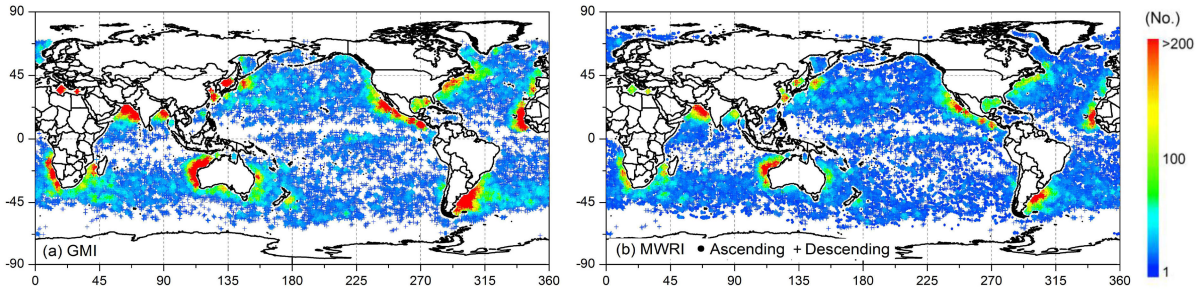

FIGURE 3. Distribution of matching TBs between satellite observation and simulation for GMI (a) and FY-3C MWRI (b), respectively.

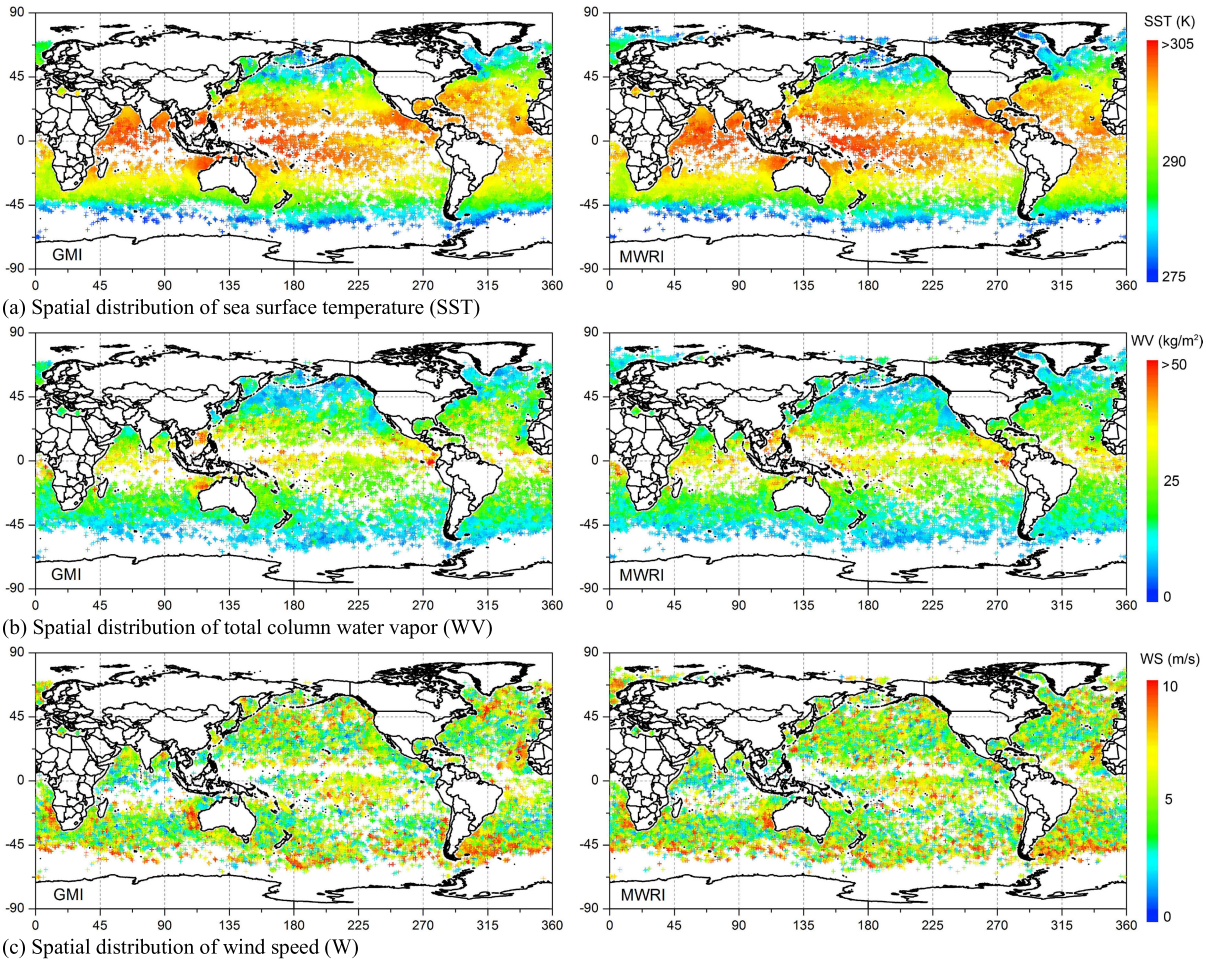

FIGURE 4. Spatial variation of sea surface temperature (a), total column water vapor (b), and wind speed (c) of the matching TBs.

observations in FY-3C MWRI channels are computed, and intercalibration coefficients are obtained.

IV. RESULTS AND ANALYSIS

A. INTERCALIBRATION RESULTS

According to the matching criteria in Section III, 127686, 78621 and 69050 matching TBs in 2017 are collected for GMI, MWRIA and MWRID, respectively. Fig. 3 displays the spatial distribution of the matching TBs. The matching TBs are mainly distributed in the Indian Ocean, Pacific Ocean and Atlantic Ocean between ±65° latitude. In higher latitude regions, only few matching TBs exist, whereas over some areas close to continents, e.g., the Australia western ocean area, the matching TBs are densely distributed (colored in red). The number of matching TBs in mid-latitude regions are larger than that in the tropical regions. The distribution of matching TBs mainly depends on satellite orbits and matching criteria. Generally, the matching TBs are uniformly distributed in the three oceans, which avoids the intercalibration to be biased to a local region.

Besides spatial distribution of matching TBs, calibration also depends on climate variables. Fig. 4 shows the spatial

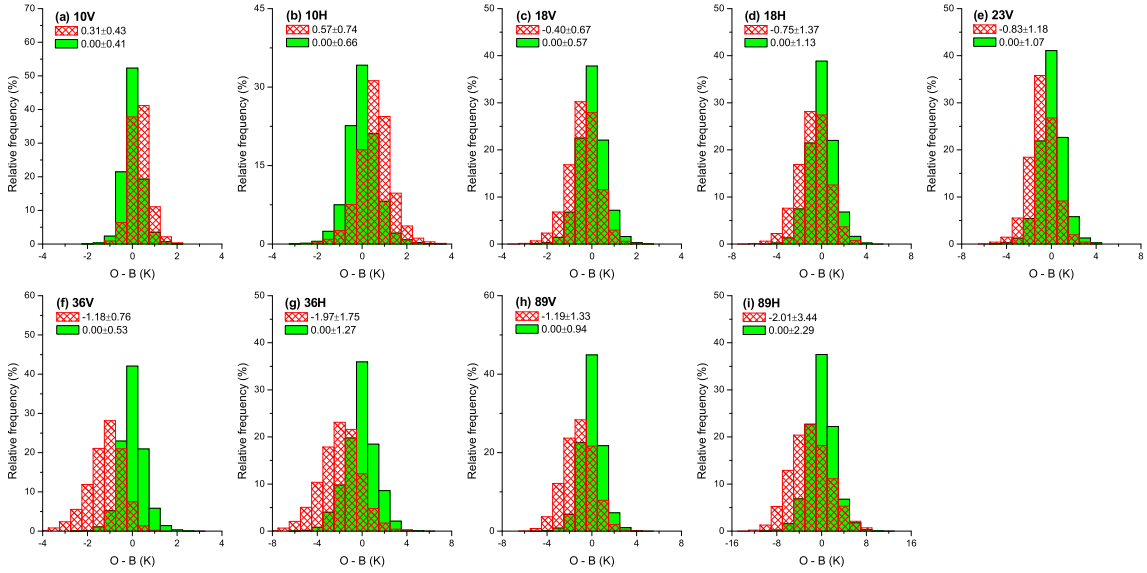

FIGURE 5. Histograms of the differences between GMI observations and simulations before (red) and after (green) removing the O-B biases.

variation of SST, WV and wind speed of the matching TBs. The SST varies from 275.0 K at higher latitude of about ±65° to 305.0 K in tropical region, and has weak dependence on longitude. The spatial variation of WV is similar to that of SST, and changes from near 0 kg/m^2 at higher latitude to approximate 50 kg/m^2 in tropical region. The spatial variation of wind speed is much more random, and has no obvious dependence on location.

To demonstrate the intercalibration procedure, the matching TBs in January 2017 are taken as examples. In the January, 10493 qualified matching TBs between GMI observations and simulations are collected. As expected, the simulations are not equal but approximate to GMI observations. Fig. 5 displays the histograms of the O-B biases between the GMI observation and simulation (colored in red). The histograms are slightly deviated from zero, and the statistical O-B biases (mean ± standard deviation at the mean) are 0.3±0.4 K, 0.6±0.7 K, −0.4±0.7 K, −0.8±1.4 K, −0.8±1.2 K, −1.2±0.8 K, −2.0±1.8 K, −1.2±1.3 K and −2.0±3.4 K in the 10V/H, 18V/H, 23V, 36V/H and 89V/H channels, respectively. The mean values of O-B biases in the low frequency channels (≤23 GHz) are less than 1.0 K, while they are less than or equal to 2.0 K in the high frequency channels. This reveals that the simulations agree with GMI observations very well, and thus the RTM can serve as a bridge between FY-3C MWRI and GMI observations. As we know, the O-B biases depend on the RTM and input climate variables. Since the GMI is the radiometric reference in this work, the O-B biases between GMI observations and simulations should be removed. Fig. 6 displays the O-B biases varying with the simulation, SST, WV, wind speed and latitude. Analysis reveals that the O-B biases between GMI observation and simulation are quadratic functions of simulations, SST, WV and latitude, whereas they are linearly related to wind speed because the wind speed is low (≤10 m/s). The black lines/curves are linear/quadratic regression results. Polynomial functions with higher order were also tested and the improvement is less than 0.15 K in average. In addition, the simulations in the nine GMI channels provide some vertical information of atmosphere, and thus the GMI observation in a channel is also highly related to the simulations in other GMI channels. According to the above analysis, the GMI observations are linear/quadratic functions of the GMI simulations and climate variables, as expressed by Eq. (10). The coefficients in Eq. (10) are determined using multiple-variable regression, and the determinant coefficients (R^2) are larger than 0.981. Because of too many coefficients, the regression results of Eq. (10) are not listed in this paper, and we will provide them if you request. Once the coefficients in Eq. (10) are obtained, the theoretical observations in GMI channels can be predicted from the simulations and climate variables. In Fig. 5, the difference histograms after removing the O-B biases are also displayed (colored in green). The green histograms are centered at zero, and the relative frequency of the histograms becomes higher (the standard deviations become smaller). This indicates that the O-B biases are removed.

In January 2017, 8905 and 7345 matching TBs are collected between FY-3C MWRI observation and simulation for ascending and descending orbits, respectively. The theoretical observations and DDs in FY-3C MWRI channels varying with the actual observations are drawn in Fig. 7. The results show that the theoretical observations and DDs in FY-3C MWRI channels are quadratic functions of the actual observations, and thus the use of Eq. (14) to describe their relation is reasonable. Except the 10H channel, the

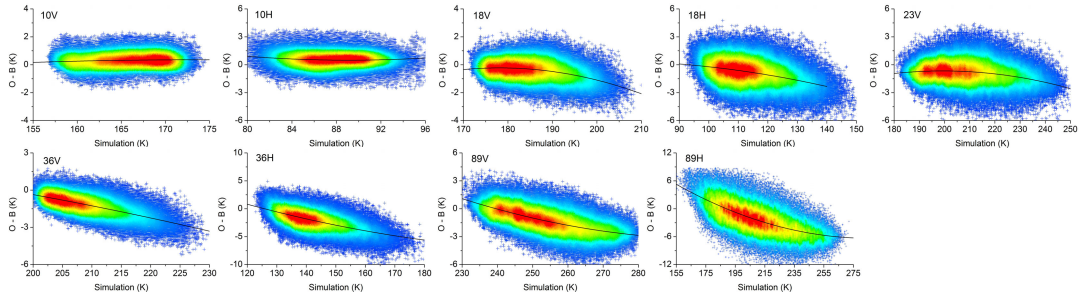

(a) O-B biases varying with the simulated brightness temperature

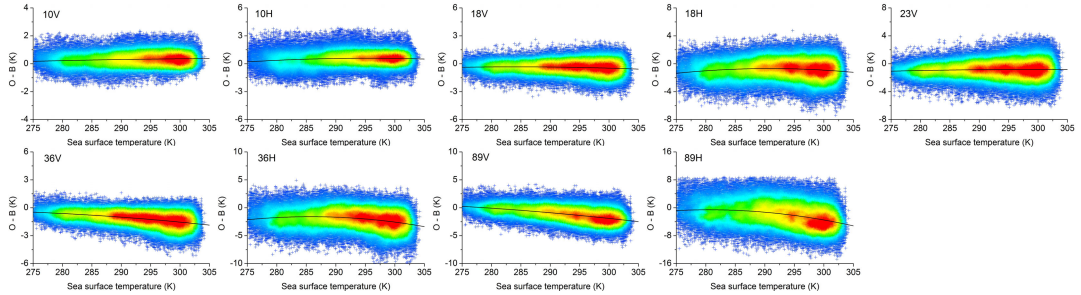

(b) O-B biases varying with sea surface temperature

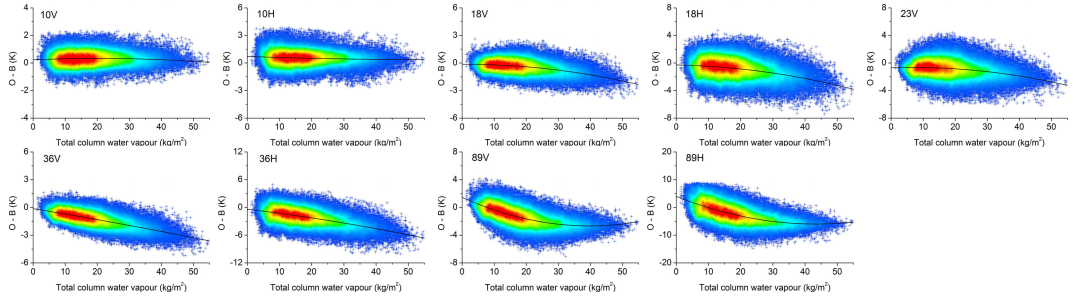

(c) O-B biases varying with total column water vapor

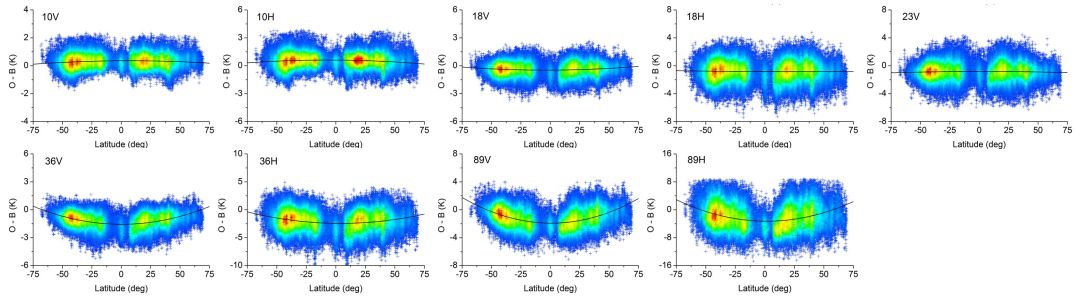

(d) O-B biases varying with latitude

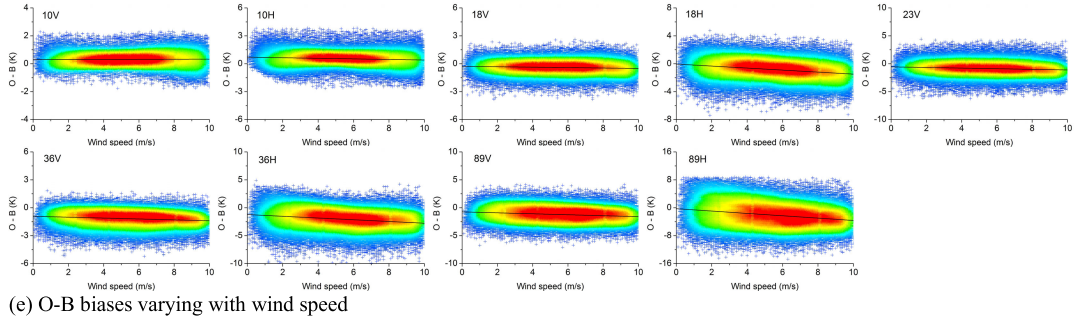

(e) O-B biases varying with wind speed

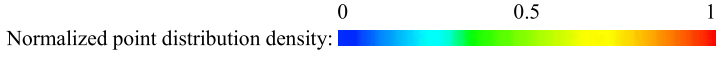

FIGURE 6. **The brightness temperature biases between GMI observation and simulation (O-B) varying with simulation (a), sea surface temperature (b), total column water vapor (c), latitude (d) and wind speed (e) (Black lines/curves are linear/quadratic regression results).**

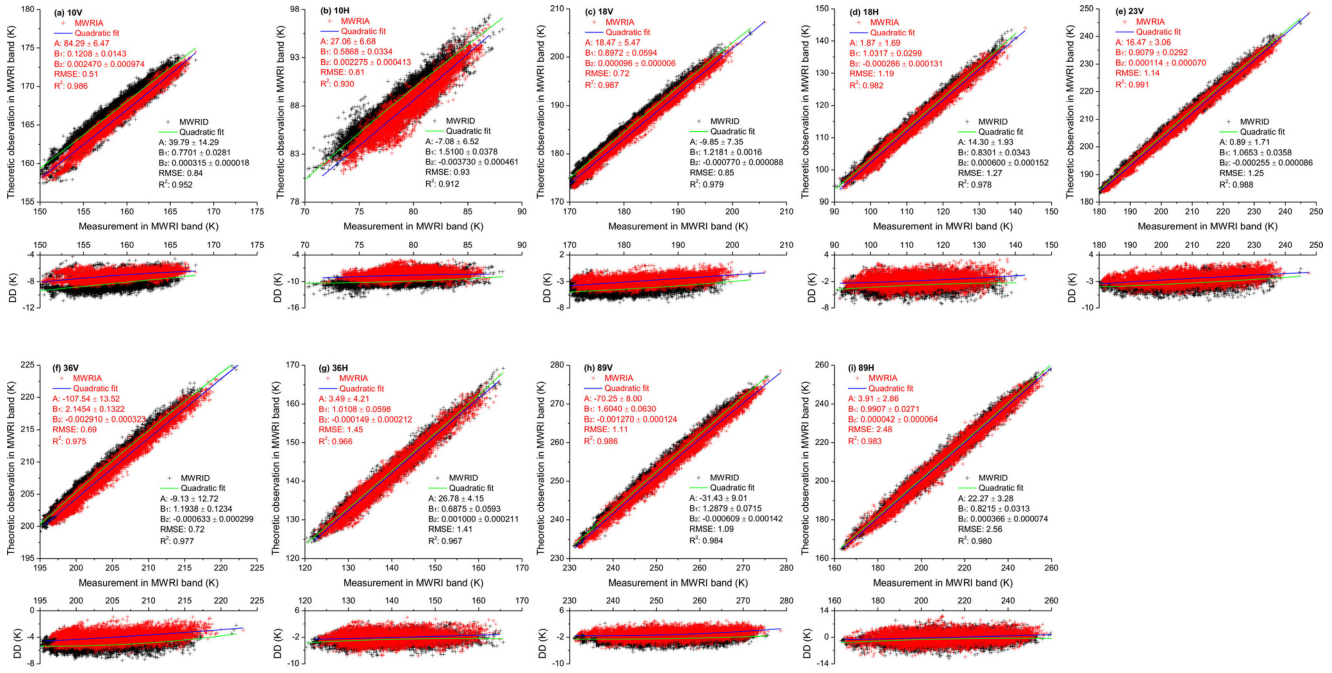

FIGURE 7. The theoretical observations and DDs in FY-3C MWRI channels obtained by the modified DD method varying with the actual measurements of FY-3C MWRI, and quadratic regression results of Eq. (14).

determinant coefficients (R^2) are larger than 0.968. The relatively lower determinant coefficients in the 10H channel, which are 0.930 and 0.912 for MWRIA and MWRID, respectively, are mainly due to the narrow dynamic range of TB. The quadratic regression results are channel-dependent, and the Root Mean Square Errors (RMSE) in the v-pol channels are generally smaller than that in the h-pol channels. For convenience, the regression results are listed in Table 3.

Overall, the MWRI observations are underestimated, and the in-orbit calibration of MWRID are worse than that of MWRIA, because the FY-3C satellite is illuminated by the Sun in descending orbits. For MWRIA, when the observation goes from the lower bound to upper bound, the mean value of DDs monotonically varies in [−8.1, −6.4] K, [−9.1, −8.3] K, [−3.8, −1.4] K, [−2.7, −0.6] K, [−3.5, −0.6] K, [−4.6, −2.6] K, [−2.6, −1.2] K, [−1.5, −0.5] K and [−1.3, 1.3] K in the channels 10V/H, 18V/H, 23V, 36V/H and 89V/H, respectively. While for MWRID, when the observation changes from the lower bound to upper bound, the mean value of DDs monotonically varies in [−9.4, 7.1] K, [−10.3, −8.9] K, [−3.8, −1.4] K, [−3.8, −2.3] K, [−4.4, −1.6] K, [−5.3, −3.5] K, [−3.6, −2.4] K, [−2.5, −1.6] K, and [−2.9, −0.6] K in the channels 10V/H, 18V/H, 23V, 36V/H and 89V/H, respectively.

In the Global Space-based Inter-Calibration System (GSICS), standard radiances of a standard scene are defined to allow comparison and convenient expression of instrument intercalibration bias in units that are understandable to users. In this work, the standard scene TBs in FY-3C MWRI channels are calculated using the RTM fed with the 1976 US standard atmosphere, a SST of 288.1 K, a wind speed of 7 m/s and a RAA of 90°, and they are 163.5, 86.5, 181.5, 110.2, 202.9, 206.1, 139.9, 247.2 and 201.5 K in the channels 10V/H, 18V/H, 23V, 36V/H and 89V/H, respectively. The calibration errors (bias ± standard deviation at the bias) of FY-3C MWRI at the standard scene TB are given in Table 4. The calibration errors at the standard scene TBs decrease with the frequency increment, and the calibration errors of MWRID are much larger than that of MWRIA. The maximum calibration error is −9.1±1.2 K in the 10H channel of MWRID, while the minimum calibration error is −0.4±2.3 K in the 89H channel of MWRIA.

B. COMPARISON WITH THE RESULTS OBTAINED BY THE DOUBLE DIFFERENCE METHOD

Although drawback exists, the DD method is still an excellent intercalibration approach. For cross-validation, the above results obtained by the modified DD method are compared with that of the DD method in the following.

For the DD method, the data are processed as follows. First, the FY-3C MWRI data, the GMI data and the ERA5 data are pixel-aggregated into a regular grid space with longitude and latitude resolutions of 1° × 1°. Then, in order to collect large number of matching TBs, the following criteria are used: (1) the pixel-aggregated MWRI observations, GMI observations, and ERA5 data are collocated over sea surfaces without sun glint under clear-sky conditions, (2) the absolute time differences between FY-3C MWRI and GMI observations are less

TABLE 3. Regression results of equation (14) For FY-3C MWRI ascending and descending orbits.

Instrument orbit	Channel name	A	B_1	B_2	RMSE (K)	R^2
MWRIA	10V	84.29±6.47	0.1208±0.0143	0.002470±0.000974	0.51	0.986
	10H	27.06±6.68	0.5868±0.0334	0.002275±0.000413	0.81	0.930
	18V	18.47±5.47	0.8972±0.0594	0.000096±0.000006	0.72	0.987
	18H	1.87±1.69	1.0317±0.0299	-0.000286±0.000131	1.19	0.982
	23V	16.47±3.06	0.9079±0.0292	0.000114±0.000070	1.14	0.991
	36V	-107.54±13.52	2.1454±0.1322	-0.002910±0.000323	0.69	0.975
	36H	3.49±4.21	1.0108±0.0598	-0.000149±0.000212	1.45	0.966
	89V	-70.25±8.00	1.6040±0.0630	-0.001270±0.000124	1.11	0.986
	89H	3.91±2.86	0.9907±0.0271	0.000042±0.000064	2.48	0.983
MWRID	10V	39.79±14.29	0.7701±0.0281	0.000315±0.0000018	0.84	0.952
	10H	-7.08±6.52	1.5100±0.0378	-0.003730±0.000461	0.93	0.912
	18V	-9.85±7.35	1.2181±0.0016	-0.000770±0.000088	0.85	0.979
	18H	14.30±1.93	0.8301±0.0343	0.000600±0.000152	1.27	0.978
	23V	0.89±1.71	1.0653±0.0358	-0.000255±0.000086	1.25	0.988
	36V	-9.13±12.72	1.1938±0.1234	-0.000633±0.000299	0.72	0.977
	36H	26.78±4.15	0.6875±0.0593	0.001000±0.000211	1.41	0.967
	89V	-31.43±9.01	1.2879±0.0715	-0.000609±0.000142	1.09	0.984
	89H	22.27±3.28	0.8215±0.0313	0.000366±0.000074	2.56	0.980

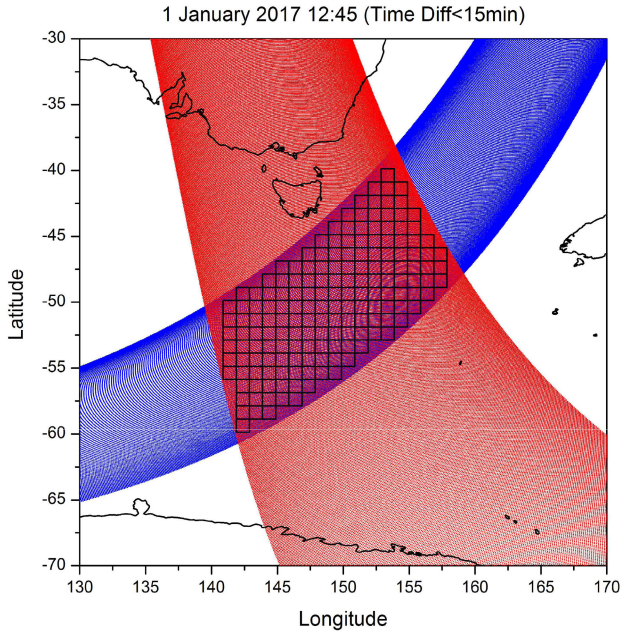

FIGURE 8. A coincident overpass between FY-3C MWRI (red dots) and GMI (blue dots) on January 1, 2017. The TBs are averaged for each sensors over 1° × 1° grid boxes as indicated by the black squares, and then screened for land, precipitation, sun glint, erroneous data, etc.

TABLE 4. Calibration Errors (Bias ± Standard deviation at the bias) in FY-3C MWRI Channels at Brightness Temperatures of the standard scene obtained by the modified double difference method.

Channel name	Standard scene TB (K)	Calibration error of MWRIA (K)	Calibration error of MWRID (K)
10V	163.5	-6.7±0.4	-7.6±0.8
10H	86.5	-8.3±0.8	-9.1±1.2
18V	181.5	-3.0±0.7	-4.4±0.8
18H	110.2	-1.9±1.0	-2.9±1.3
23V	202.9	-2.5±1.1	-3.6±1.2
36V	206.1	-3.9±0.8	-5.1±0.8
36H	139.9	-2.1±1.5	-2.6±1.4
89V	247.2	-1.5±1.0	-2.5±1.1
89H	201.5	-0.4±2.3	-1.2±2.5

than 60 minutes, and (3) the time-nearest ERA5 data of both FY-3C MWRI and GMI observations are identical. Because of the use of large time window (60 min), only the ERA5 data at the Coordinated Universal Time (UTC) of 0:00, 3:00, 6:00, 9:00, 12:00, 15:00, 18:00 and 21:00 are used. As mentioned above, the clear-sky criterion that the ERA5 total cloud cover is zero over a 1° × 1° grid is too strict to collect large number of matching TBs. Therefore, the clear-sky criterion is lowered, and a pixel-aggregated grid (1° × 1°) is labeled clear-sky only if the maximum relative humidity of all the ERA5 grids (0.25° × 0.25°) fallen into the pixel-aggregated grid (1° × 1°) is less than 95%. Meanwhile, the empirical filters [21]–[23] are also used together to screen out cloud-contaminated observations. Fig. 8 shows an example of coincident overpass between FY-3C MWRI and GMI over the 1° × 1° grid space on January 1 2017. Next, the TBs in FY-3C MWRI and GMI channels are simulated using the RTM fed with the ERA5 data over the qualified matching grids. Afterward, the DDs and theoretical observations in FY-3C MWRI channels are calculated. Finally, the intercalibration coefficients in Eq. (14) are obtained.

With the above criteria, 7401 and 6278 matching TBs are collected between GMI and FY-3C MWRI for ascending and descending orbits, respectively. Fig. 9 displays the DDs and theoretical observations in FY-3C MWRI channels obtained by the DD method varying with the actual observations of FY-3C MWRI. Because the wind speed is not limited, the dynamic ranges of FY-3C MWRI observations are 3∼5 K larger than that in Fig. 7. Similar to the results in Fig. 7 obtained by the modified DD method, the theoretical observations and DDs in Fig. 9 are also

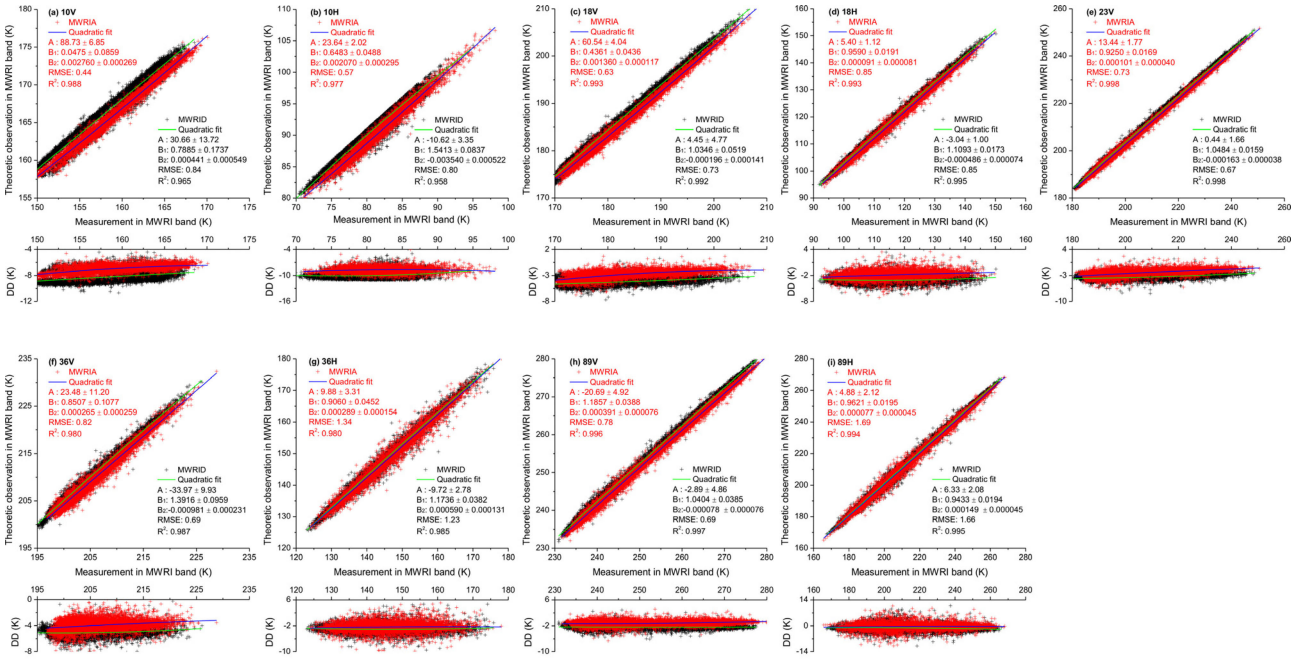

FIGURE 9. The theoretical observations and DDs in FY-3C MWRI channels obtained by the DD method varying with the FY-3C MWRI actual observations, and the quadratic regression results (A, B_1 and B_2 are coefficients of Eq. (14)).

TABLE 5. Comparison of calibration errors (bias ± standard deviation at the bias) in FY-3C MWRI channels at standard scene TB.

Channel name	Standard scene TB (K)	Calibration error of MWRIA (K)		Calibration error of MWRID (K)	
		The modified DD method	The DD method	The modified DD method	The DD method
10V	163.5	-6.7±0.4	-6.7±0.3	-7.6±0.8	-7.9±0.7
10H	86.5	-8.3±0.8	-8.7±0.7	-9.1±1.2	-9.7±0.9
18V	181.5	-3.0±0.7	-2.9±0.7	-4.4±0.8	-4.3±0.9
18H	110.2	-1.9±1.0	-2.0±0.8	-2.9±1.3	-3.0±0.8
23V	202.9	-2.5±1.1	-2.4±0.7	-3.6±1.2	-3.5±0.9
36V	206.1	-3.9±0.8	-4.0±0.8	-5.1±0.8	-5.1±0.8
36H	139.9	-2.1±1.5	-2.4±1.4	-2.6±1.4	-3.0±1.1
89V	247.2	-1.5±1.0	-1.3±1.0	-2.5±1.1	-2.4±0.6
89H	201.5	-0.4±2.3	-0.4±1.8	-1.2±2.5	-1.0±2.1

quadratic functions of the actual observations. The regression results are channel-dependent: all the determinant coefficients (R^2) are larger than 0.958, and the RMSEs in the v-pol channels are smaller than that in the h-pol channels. Generally, the MWRI observations are underestimated (DD<0), and the in-orbit calibration of MWRID are worse than that of MWRIA. Generally, the results obtained by the DD method and the modified DD method are qualitatively consistent.

To quantitatively compare the results, the calibration errors (bias ± standard deviation at the bias) at the standard scene TBs obtained by the DD method are calculated and listed in Table 5. For convenience, the calibration errors obtained by the modified DD method are also given in Table 5. Except the 10H, the differences between the mean biases obtained by the two methods do not exceed 0.2 K. In the 10H, the differences are 0.4 K and 0.6 K for MWRIA and MWRID, respectively. The relatively large differences in the 10H channel between the two methods are attributed to the fact that the standard scene TB in the 10H channel (86.5 K) is located at the upper edge of the TB range obtained by the modified DD method, and the results may be unreliable. The standard deviations of the modified DD method are generally 0.1∼0.5 K larger than that of the DD method. This is mainly due to the large grid sizes (1° × 1°) used by the DD method. Totally, the results of the two methods are quantitatively consistent, and the modified DD method does not have obvious advantage over the DD method. The main downside of the modified DD method lies on the multiple-variable regression given by Eq. (10).

C. MONTHLY VARIATION OF INTERCALIBRATION

Besides the January, intercalibration of FY-3C MWRI against GMI in other months of 2017 is also accomplished to investigate the monthly variation.

Fig. 10 shows the box chart of the monthly mean and standard deviation of the O-B biases in GMI channels at the standard scene TBs in 2017. Both the monthly mean and standard deviation at the standard scene TBs increase with frequency, and the two statistical parameters in the h-pol channels are basically larger than that in the v-pol channels. Most of the monthly mean values are distributed in [−1.0, 1.0] K, and the variation is less than 0.6 K except the 89H channel, in which the variation is up to 1.2 K. Generally, both the monthly mean and standard deviation of the O-B biases

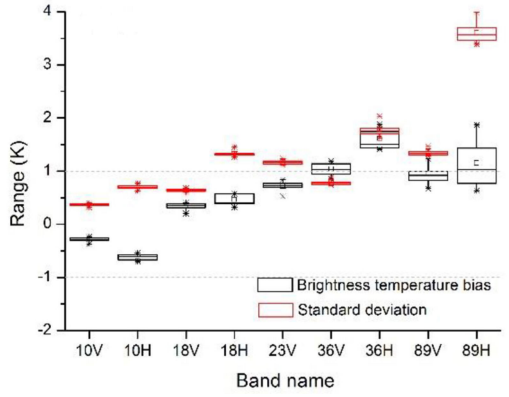

FIGURE 10. Box chart of the monthly mean and standard deviation of the O-B biases in GMI channels at brightness temperature of the standard scene in 2017 (rectangle denotes interquartile range between 25% and 75%; little square and horizontal line segment stand for mean and median values, respectively; symbol ∗ represents maximum and minimum values).

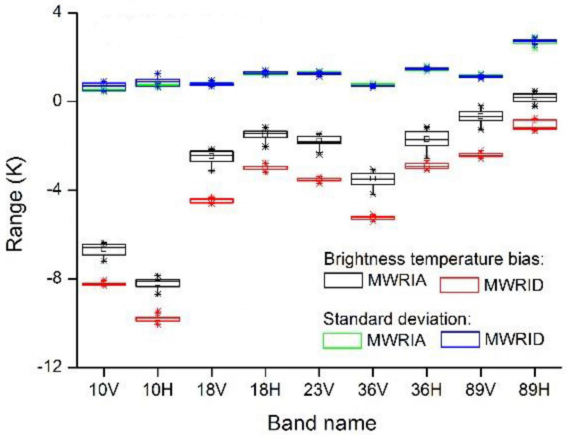

FIGURE 11. Box chart of monthly calibration biases and standard deviations in FY-3C MWRI channels at brightness temperatures of the standard scene in 2017 (rectangle denotes interquartile range between 25% and 75%; little square and horizontal line segment stand for mean and median values, respectively; symbol ∗ represents maximum and minimum values).

in GMI channels at the standard scene TBs are stable, and the simulations agree with GMI observations very well in the whole year.

Fig. 11 displays the box chart of monthly mean and standard deviation of the DDs in FY-3C MWRI channels at the standard scene TBs in 2017. Generally, the calibration bias (mean of DDs) at the standard scene TBs decreases with frequency from about −9.5 K in the 10H channel for MWRID to approximately 0.4 K in the 89H channel for MWRIA, and the calibration biases of MWRID are larger than that of MWRIA. Whereas, the standard deviations slightly increase with frequency. The variations of both calibration biases and standard deviations at the standard scene TBs are less than 0.6 K. This means that, although calibration biases exist in the MWRI channels, the monthly calibration biases and standard deviations are quite stable in 2017. Due to length limit, the intercalibration coefficients in February to December of 2017 are not listed in this paper, and we will provide them to you through personal communication.

V. CONCLUSION AND DISCUSSION

This paper addressed the intercalibration of FY-3C MWRI against GMI, in which the modified DD method was developed and the TBs in FY-3C MWRI and GMI channels were simulated using the ocean microwave RTM fed with the ERA5 data.

Generally, the MWRI observations are underestimated, especially for the low frequency channels, and the calibration of MWRID is relatively 1∼2 K worse than that of MWRIA. The calibration errors in FY-3C MWRI channels are temperature-dependent, and they are quadratic functions of the MWRI observations. At the standard scene TBs, for MWRIA, the calibration errors (bias ± standard deviation at the bias) are −6.7±0.4 K, −8.3±0.8 K, −3.0±0.7 K, −1.9±1.0 K, −2.5±1.1 K, −3.9±0.8 K, −2.1±1.5 K, −1.5±1.0 K and −0.4±2.3 K in the 10V/H, 18V/H, 23V, 36V/H and 89V/H channels, respectively. Whereas for MWRID, the calibration errors are −7.6±0.8 K, −9.1±1.2 K, −4.4±0.8 K, −2.9±1.3 K, −3.6±1.2 K, −5.1±0.8 K, −2.6±1.4 K, −2.5±1.1 K and −1.2±2.5 K in the nine channels, respectively. Although calibration errors exist, the in-orbit calibration of FY-3C MWRI is stable in 2017. The results obtained by the modified DD method are quantitatively consistent with that of the DD method. This means that the modified DD method developed in this work is valid.

Contrary to the traditional DD method, the modified DD method does not require coincident observations between two radiometers, thus it can collect large number of qualified matching TBs with much stricter criteria in a short period. It is promising to be applied to intercalibration with both target and reference radiometers on polar-orbiting satellites. The main downside of the modified DD method in this work lies on the multiple-variable regression given by Eq. (10). In the future, we will collect more than five years of matching TBs between GMI observation and simulation, and then remove the O-B biases using deep learning technique.

ACKNOWLEDGMENT

The authors would like to thank the anonymous reviewers for their constructive comments, which helped us to improve the quality and presentation of this article.

REFERENCES

[1] J. Yang, P. Zhang, N. Lu, Z. Yang, J. Shi, and C. Dong, "Improvements on global meteorological observations from the current Fengyun 3 satellites and beyond," *Int. J. Digit. Earth*, vol. 5, no. 3, pp. 251–265, May 2012.

[2] F. Tang, X. Zou, H. Yang, and F. Weng, "Estimation and correction of geolocation errors in FengYun-3C microwave radiation imager data," *IEEE Trans. Geosci. Remote Sens.*, vol. 54, no. 1, pp. 407–420, Jan. 2016.

[3] S. Wu and J. Chen, "Instrument performance and cross calibration of FY-3C MWRI," in *Proc. IEEE Int. Geosci. Remote Sens. Symp. (IGARSS)*, Beijing, China, Jul. 2016, pp. 388–391.

[4] D. Newell, D. Draper, Q. Remund, D. Figgins, S. Krimchansky, F. Wentz, and T. Meissner, "GPM microwave imager (GMI) on-orbit performance and calibration results," in *Proc. IEEE Int. Geosci. Remote Sens. Symp. (IGARSS)*, Milan, Italy, Jul. 2015, pp. 5158–5161.
[5] D. Draper, D. Newell, and F. Wentz, "Global precipitation measurement microwave imager (GMI) on-orbit calibration," in *Proc. 14th Specialist Meeting Microw. Radiometry Remote Sens. Environ. (MicroRad)*, Apr. 2016, pp. 166–169.
[6] W. Berg, S. Bilanow, R. Chen, S. Datta, D. Draper, H. Ebrahimi, S. Farrar, W. L. Jones, R. Kroodsma, D. McKague, V. Payne, J. Wang, T. Wilheit, and J. X. Yang, "Intercalibration of the GPM microwave radiometer constellation," *J. Atmos. Ocean. Technol.*, vol. 33, no. 12, pp. 2639–2654, Dec. 2016.
[7] A. Asem, P. Y. Deschamps, and D. Ho, "Calibration of METEOSAT infrared radiometer using split window channels of NOAA AVHRR," *J. Atmos. Ocean. Technol.*, vol. 4, no. 4, pp. 553–562, Dec. 1987.
[8] G. Chander, T. J. Hewison, N. Fox, X. Wu, X. Xiong, and W. J. Blackwell, "Overview of intercalibration of satellite instruments," *IEEE Trans. Geosci. Remote Sens.*, vol. 51, no. 3, pp. 1056–1080, Mar. 2013.
[9] T. J. Hewison, X. Wu, F. Yu, Y. Tahara, X. Hu, D. Kim, and M. Koenig, "GSICS inter-calibration of infrared channels of geostationary imagers using Metop/IASI," *IEEE Trans. Geosci. Remote Sens.*, vol. 51, no. 3, pp. 1160–1170, Mar. 2013.
[10] D. R. Doelling, P. Minnis, and L. Nguyen, "Calibration comparisons between SEVIRI, MODIS and GOES data," in *Proc. 2nd MSG-RAO Workshop, Salzburg, Austria, Sep. 9-10*, vol. 2004, pp. 149–154.
[11] G.-M. Jiang, H. Yan, and L.-L. Ma, "Intercalibration of SVISSR/FY-2C infrared channels against MODIS/Terra and AIRS/Aqua channels," *IEEE Trans. Geosci. Remote Sens.*, vol. 47, no. 5, pp. 1548–1558, May 2009.
[12] G.-M. Jiang and Z.-L. Li, "Cross-calibration of MSG1-SEVIRI infrared channels with terra-MODIS channels," *Int. J. Remote Sens.*, vol. 30, no. 30, pp. 753–769, Feb. 2009.
[13] G.-M. Jiang, Z.-Y. Wang, and J. Wang, "Inter-calibration of VIRR/FY-3A/B split-window channels with AIRS/Aqua and IASI/Metop-a measurements," *Int. J. Remote Sens.*, vol. 37, no. 22, pp. 5249–5269, Nov. 2016.
[14] G.-M. Jiang, S. Li, and Z.-Y. Wang, "Intercalibration of IRAS/FY-3B infrared channels with IASI/Metop-a 1C data," *IEEE J. Sel. Topics Appl. Earth Observ. Remote Sens.*, vol. 10, no. 6, pp. 2510–2517, Jun. 2017.
[15] W.-X. Li, G.-M. Jiang, G. Li, and C. Li, "Intercalibration of advanced himawari imager's infrared channels with IASI/Metop-B 1C data," *IEEE J. Sel. Topics Appl. Earth Observ. Remote Sens.*, vol. 11, no. 6, pp. 1989–1996, Jun. 2018.
[16] L. Wang, M. Goldberg, X. Wu, C. Cao, R. A. Iacovazzi, F. Yu, and Y. Li, "Consistency assessment of atmospheric infrared sounder and infrared atmospheric sounding interferometer radiances: Double differences versus simultaneous nadir overpasses," *J. Geophys. Res.*, vol. 116, no. 11, 2011, Art. no. D11111.
[17] S. K. Biswas, S. Farrar, K. Gopalan, A. Santos-Garcia, W. L. Jones, and S. Bilanow, "Intercalibration of microwave radiometer brightness temperatures for the global precipitation measurement mission," *IEEE Trans. Geosci. Remote Sens.*, vol. 51, no. 3, pp. 1465–1477, Mar. 2013.
[18] C. S. Ruf, "Detection of calibration drifts in spaceborne microwave radiometers using a vicarious cold reference," *IEEE Trans. Geosci. Remote Sens.*, vol. 38, no. 1, pp. 44–52, Jan. 2000.
[19] R. A. Kroodsma, D. S. McKague, and C. S. Ruf, "Inter-calibration of microwave radiometers using the vicarious cold calibration double difference method," *IEEE J. Sel. Topics Appl. Earth Observ. Remote Sens.*, vol. 5, no. 3, pp. 1006–1013, Jun. 2012.
[20] R. A. Kroodsma, D. S. McKague, and C. S. Ruf, "Vicarious cold calibration for conical scanning microwave imagers," *IEEE Trans. Geosci. Remote Sens.*, vol. 55, no. 2, pp. 816–827, Feb. 2017.
[21] A. P. Stogryn, C. T. Butler, and T. J. Bartolac, "Ocean surface wind retrievals from special sensor microwave imager data with neural networks," *J. Geophys. Res.*, vol. 99, no. C1, pp. 981–984, 1994.
[22] S. T. Brown and C. S. Ruf, "Determination of an amazon hot reference target for the on-orbit calibration of microwave radiometers," *J. Atmos. Ocean. Technol.*, vol. 22, no. 9, pp. 1340–1352, Sep. 2005.
[23] J. X. Yang, D. S. McKague, and C. S. Ruf, "Uncertainties in radiometer intercalibration associated with variability in geophysical parameters," *J. Geophys. Res., Atmos.*, vol. 121, no. 19, pp. 11348–11367, Oct. 2016.
[24] F. J. Wentz, "A model function for ocean microwave brightness temperatures," *J. Geophys. Res.*, vol. 88, no. C3, pp. 1892–1908, 1983.
[25] F. J. Wentz, "A well-calibrated ocean algorithm for special sensor microwave/imager," *J. Geophys. Res., Oceans*, vol. 102, no. C4, pp. 8703–8718, Apr. 1997.
[26] T. Meissner and F. Wentz, "An updated analysis of the ocean surface wind direction signal in passive microwave brightness temperatures," *IEEE Trans. Geosci. Remote Sens.*, vol. 40, no. 6, pp. 1230–1240, Jun. 2002.
[27] T. Meissner and F. J. Wentz, "A radiative transfer model function for 85.5 GHz special sensor microwave imager ocean brightness temperatures," *Radio Sci.*, vol. 38, no. 4, p. 8066, Aug. 2003.
[28] T. Meissner and F. J. Wentz, "The complex dielectric constant of pure and sea water from microwave satellite observations," *IEEE Trans. Geosci. Remote Sens.*, vol. 42, no. 9, pp. 1836–1849, Sep. 2004.
[29] T. Meissner and F. J. Wentz, "The emissivity of the ocean surface between 6 and 90 GHz over a large range of wind speeds and Earth incidence angles," *IEEE Trans. Geosci. Remote Sens.*, vol. 50, no. 8, pp. 3004–3026, Aug. 2012.
[30] F. J. Wentz and T. Meissner, "Atmospheric absorption model for dry air and water vapor at microwave frequencies below 100 GHz derived from spaceborne radiometer observations," *Radio Sci.*, vol. 51, no. 5, pp. 381–391, May 2016.
[31] F. J. Wentz and T. Meissner, "AMSR ocean algorithm, version 2," Remote Sens. Syst., Santa Rosa, CA, USA, Tech. Rep. 121599A-1, 2000. [Online]. Available: http://www.remss.com/papers/amsr/AMSR_Ocean_Algorithm_Version_2.pdf
[32] J. R. Waters, *Absorption and Emission by Atmospheric Gases, in Methods of Experimental Physics*, vol. 12B, M. L. Meeks, Eds. Orlando, FL, USA: Academic, 1976, ch. 2.3.
[33] H. J. Liebe, "An updated model for millimeter wave propagation in moist air," *Radio Sci.*, vol. 20, no. 5, pp. 1069–1089, Sep. 1985.
[34] H. J. Liebe, "MPM—An atmospheric millimeter-wave propagation model," *Int. J. Infr. Millim. Waves*, vol. 10, no. 6, pp. 631–650, Jun. 1989.
[35] H. J. Liebe, G. A. Hufford, and M. G. Cotton, "Propagation modeling of moist air and suspended water/ice particles at frequencies below 1000 GHz," in *Proc. AGARD Conf. Proc.*, vol. 542, 1993, pp. 3.1–3.10.
[36] P. W. Rosenkranz, "Water vapor microwave continuum absorption: A comparison of measurements and models," *Radio Sci.*, vol. 33, no. 4, pp. 919–928, Jul. 1998.
[37] S. T. Wu and A. K. Fung, "A noncoherent model for microwave emissions and backscattering from the sea surface," *J. Geophys. Res.*, vol. 77, no. 30, pp. 5917–5929, 1972.
[38] F. J. Wentz, "A two-scale scattering model for foam-free sea microwave brightness temperatures," *J. Geophys. Res.*, vol. 80, no. 24, pp. 3441–3446, Aug. 1975.
[39] S. H. Yueh, "Modeling of wind direction signals in polarimetric sea surface brightness temperatures," *IEEE Trans. Geosci. Remote Sens.*, vol. 35, no. 6, pp. 1400–1418, Nov. 1997.
[40] K. M. St. Germain, G. Poe, and P. Gaiser, "Modeling of the polarimetric microwave signal due to ocean surface wind vector," in *Proc. IGARSS . Sens. Manag. Environment. IEEE Int. Geosci. Remote Sensing. Symp.*, Seattle, WA, USA, vol. 5, Jul. 998, pp. 2304–2306.
[41] J. T. Johnson, "An efficient two-scale model for the computation of thermal emission and atmospheric reflection from the sea surface," *IEEE Trans. Geosci. Remote Sens.*, vol. 44, no. 3, pp. 560–568, Mar. 2006.
[42] E. E. Borbas, S. W. Seemann, H.-L. Huang, J. Li, and W. P. Menzel, "Global profile training database for satellite regression retrievals with estimates of skin temperature and emissivity," in *Proc. 14th Int. ATOVS Study Conf. (CIMSS)*, Madison, WI, USA, 2005, pp. 763–770.
[43] R. Chen, H. Ebrahimi, and W. L. Jones, "Creating a multidecadal ocean microwave brightness dataset: Three-way intersatellite radiometric calibration among GMI, TMI, and WindSat," *IEEE J. Sel. Topics Appl. Earth Observ. Remote Sens.*, vol. 10, no. 6, pp. 2623–2630, Jun. 2017.
[44] Q. F. Lu, H. Lawrence, N. Bormann, S. English, K. Lean, N. Atkinson, W. Bell, and F. Carminati, "An evaluation of FY-3C satellite data quality at ECMWF and the met office," ECMWF, Reading, U.K., ECMWF Tech. Memoranda 767, 2015.
[45] M. Zhang, Q. Lu, S. Gu, X. Hu, and S. Wu, "Analysis and correction of the difference between the ascending and descending orbits of the FY-3C microwave imager," *J. Remote Sens.*, vol. 23, no. 5, pp. 841–849, 2019.

ZI-QIAN ZENG (Student Member, IEEE) received the B.S. degree in electronic information science and technology from the Wuhan University of Technology, Wuhan, China, in 2017. She is currently pursuing the M.S. degree in electromagnetic field and microwave technology with the Key Laboratory for Information Science of Electromagnetic Waves (Ministry of Education), Fudan University, Shanghai, China.

Her research mainly focuses on the intercalibration of satellite microwave imagers.

GENG-MING JIANG (Member, IEEE) received the B.S. degree in photogrammetric engineering and remote sensing from the Wuhan Technical University of Surveying and Mapping, Wuhan, China, in 1997, the M.S. degree in cartography and geographical information system from the Institute of Remote Sensing Applications, Chinese Academy of Sciences, Beijing, China, in 2003, and the Ph.D. degree in remote sensing from Université Louis Pasteur, Strasbourg, France, in 2007.

He is currently an Associate Professor with the Key Laboratory for Information Science of Electromagnetic Waves (Ministry of Education), Fudan University, Shanghai, China. His research interests mainly focus on intercalibration of satellite instruments, quantitative remote sensing, and digital image processing.